

Submitted to *Cryogenics* on September 24, 2018
Revised on January 13, 2019

Multidisciplinary analysis of the transient performance of a 20 kW class HTS
induction/synchronous motor cooled with a cryocooler and gaseous air-gap coolant

T. Karashima¹, T. Nakamura^{*1} and M. Okuno¹

1. Department of Electrical Engineering, Graduate School of Engineering, Kyoto University,
Kyoto-Daigaku-Katsura, Nishikyo-Ku, Kyoto 615-8510, Japan

Abstract

This paper presents a multidisciplinary analysis procedure for the transient cooling and rotating characteristics of a 20 kW class high temperature superconducting (HTS) induction/synchronous motor, this analysis couples the nonlinear voltage equations, equation of motion, and a thermal equivalent circuit. First, the quantitative accuracy of the thermal equivalent circuit is validated through comparison with results obtained using the 3D finite element analysis. Then, multidisciplinary analysis is performed with the assumption that the outer surface of the stator is cooled by a cryocooler and the air-gap between the stator and rotor is cooled by a gaseous coolant. It is demonstrated that the transient performance of the motor can be fully determined using our developed procedure. For instance, we can determine the gas-flow speed in the air-gap required for cooling of the HTS rotor, by assuming appropriate expressions for the heat transfer in the air-gap. The analysis procedure and obtained results are effective for investigation of the variable speed performance of an HTS motor system and for optimal design of the motor cooling structure and method.

Keywords: high temperature superconducting induction/synchronous motor; multidisciplinary analysis; cryocooler; gaseous coolant; transient characteristics

*Corresponding Author:

Taketsune Nakamura

Postal address:

Department of Electrical Engineering, Graduate School of Engineering, Kyoto University,
Kyoto-Daigaku-Katsura, Nishikyo-Ku, Kyoto 615-8510, Japan

Tel: +81-75-383-3117

Fax: +81-75-383-3090

E-mail: nakamura.taketsune.2a@kyoto-u.ac.jp

1. Introduction

Implementation in a rotating motor is one of the promising applications of a high temperature superconductor (HTS). In particular, transportation equipment, e.g., ships, airplanes, buses, and trucks, is the primary target for such applications.

Various studies on the ship propulsion HTS motor have been performed internationally [1–8]. The typical rotational speed of a conventional ship propulsion motor is lower than that of an HTS motor by several hundred rpm, and the Joule-type power loss is, correspondingly, larger. Therefore, reduction of such dissipation is highly important for realisation of a highly efficient motor, and the HTS motor is a powerful candidate. American Superconductor (AMSC) group (USA) has reported pioneering work on ship propulsion motors [1,2], finally developing the world's largest 36.5 MW synchronous motor. In this motor, the HTS field winding is cooled by means of gaseous helium, and those researchers have also succeeded in implementing a full load test [2]. Researchers at Siemens (Germany) have developed a 400 kW class synchronous motor, in which the HTS rotor is cooled by a Gifford-McMahon cryocooler (30 W@25 K) [3]. They have successfully performed various tests over a period of almost 1.5 years, and demonstrated the possibility of long term operation of an HTS motor. Furthermore, the IHI group (Japan) has developed a 12.5 kW class fully superconducting axial-gap motor, and has moved to manufacture a 400 kW class motor that consists of an HTS stator and a permanent magnet rotor [4]. In their motor, the HTS windings are cooled with circulating liquid nitrogen. The Kawasaki Heavy Industries group (Japan) has successfully completed development of a 3 MW class ship propulsion motor, in which the HTS field windings are cooled by circulating helium gas [5]. In addition, the Doosan Heavy Industries & Construction group (Korea) has been developing a MW class ship propulsion motor using rare-earth barium copper oxide (REBCO) tapes [6]. Finally, a research group at Tokyo University of Marine Science and Technology (Japan) has attempted to apply a bulk HTS in a ship propulsion

motor [7]. Those researchers have also succeeded in fabricating a compact rotary joint, which allows introduction of liquid cryogen into the HTS rotor [8].

For aircraft applications, the power density (mechanical output per unit mass) is important, and higher speed motors, e.g., with several hundred rpm, have been targeted [9-13]. Although only a limited number of conceptual design studies have been performed, realisation of a high-speed motor is very attractive for advancing the new possibility of an HTS motor. Researchers at Florida A&M University-Florida State University and their collaborators (USA) have actively reported concepts and design results for an HTS motor system for aircraft applications [9, 10]. Furthermore, researchers at Airbus Group Innovations and their collaborators (UK), and at Leibniz University-Braunschweig University of Technology (Germany), have separately studied conceptual designs of a distributed aircraft propulsion system using an HTS motor/generator [11] and a hybrid electric aircraft using HTS rotating machines [12], respectively. Finally, researchers at the University of Tokyo (Japan) have reported detailed electromagnetic design results for an HTS synchronous motor [13].

For land transport equipment, generation of a higher torque in a limited space is required. The mechanical output target range is a few hundred kW, and a compact, high-efficiency cryocooler is mandatory for practical application. Researchers at Sumitomo Electric Industries (Japan) has developed a series-connected direct-current (DC) motor, in which liquid nitrogen cooled bismuth strontium calcium copper oxide (BSCCO) pancake field coils are adopted [14]. This motor has been mounted on a middle class passenger car, and an actual running test has been successfully performed. In addition, researchers at Sumitomo Heavy Industries, Ltd. (Japan) have developed a Stirling cryocooler for an HTS electric bus [15]. The reported cooling power and coefficient of performance (COP) are, respectively, 151 W and 0.07 at 70 K. The present authors' group (at Kyoto University, with collaborators) (Japan) has been developing a 20 kW class HTS induction/synchronous motor (HTS-ISM) for transportation equipment such as buses, trucks, and

middle class car [16]. Recently, we have validated the highly efficient regeneration characteristics [17] and excellent controllability [18] of this motor.

To realise a practical HTS-ISM motor system, the cooling structure and method must to be optimised to facilitate a smaller casing (cryostat) with effective cooling capability. Although the above-mentioned 20 kW class HTS-ISM is currently cooled by liquid nitrogen [16-18], our final target is realisation of a system cooled by a cryocooler and gaseous coolant, e.g., helium or neon.

In this paper, a quantitative analysis procedure for the transient cooling and rotating characteristics of a 20 kW class HTS-ISM is developed. First, we develop a thermal analysis procedure based on a thermal equivalent circuit; the accuracy of this procedure is validated by comparison with results obtained via the 3D finite element analysis (3D-FEA). Then, we couple the equations of the above procedure with nonlinear voltage equations and the equation of motion, and multidisciplinary analysis is performed for the transient rotation and cooling characteristics of the motor. Here, it is assumed that the outermost surface of the stator is cooled by a cryocooler and the air-gap between the stator and rotor is cooled by a gaseous coolant. By assuming appropriate heat transfer characteristics for the air-gap gaseous cooling, analysis results for the transient characteristics are obtained and discussed.

2. Subject motor

2.1 Structure and specifications

Fig. 1 shows photographs of the fabricated 20 kW class prototype HTS-ISM (3-phase, 4-pole) [16-18]. Rotor windings are formed by using Bi-2223 superconducting tapes whereas stator windings employ conventional copper wires. Laminated silicon steels were utilised for both cores of the rotor and stator, and stainless steel (SUS304) was utilised for the shaft. Table I lists the motor

specifications. A more detailed explanation can be found in [16].



(a) HTS rotor



(b) Cu stator

Fig. 1 Photographs of 20 kW class HTS-ISM [16-18]

Table I Technical specifications of 20 kW class HTS-ISM [16-18]

Item	Stator	Rotor
Pole number	4	n/a
Slot number	48	38
Outer diameter	200.0 mm	119.3 mm
Inner diameter	120.0 mm	50.0 mm
Length	106.0 mm	106.0 mm
Weight	16.0 kg	13.6 kg
Coil material	Cu	Bi-2223 (HTS)
Turn number/coil	32	n/a

2.2 HTS tape current transport property

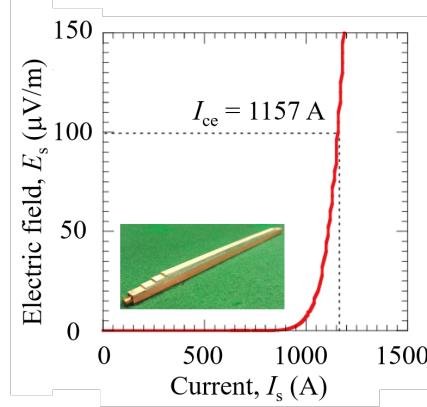


Fig. 2 Electric field, E_s , vs. current, I_s , curve of an HTS rotor bar at 77 K, obtained from measured results (inset: Bi-2223 rotor bar) [18]

Fig. 2 shows an electric field, E_s , vs. current, I_s , curve measured for an HTS rotor bar (inset), which was installed in an iron core at 77 K [18]. The E_s - I_s (flux-flow) curve can be expressed by the following equation:

$$E_s(I_s) = A(I_s - I_{cm})^n \quad (1)$$

where I_{cm} (= 694 A) is the critical current that yields exactly zero resistance, and A and n are a coefficient and the power-law index, respectively. Further, the temperature dependence of the above E - I curve is considered to be that of I_{cm} , which is expressed as follows [19]:

$$I_{cm} \propto \left(1 - \frac{T}{T_{ir}}\right)^{2\nu} \quad (2)$$

where T_{ir} (= 105 K) is the so-called irreversibility temperature, and ν (= 0.5) is the static critical component. It should be noted that the critical current (I_{ce}), which is defined by the typical electric field criterion of 100 $\mu\text{V/m}$, is 1157 A; however, I_{cm} is always less than I_{ce} .

The superconducting layer resistance, R_s , is defined as E_s/lI_s , where l denotes the HTS rotor winding length. Moreover, the HTS rotor windings consisted of not only a superconducting layer but also a normal conducting layer. That is, the Bi-2223 tape included a normal conducting layer

(Ag or its alloy), which is crucial for production of high quality tape. The resistance of this layer, R_{ag} , also acted as the so-called stability resistance, and the accidental over current I_{ov} bypassed the superconducting layer if I_{ov} was larger than I_{ce} . The HTS windings further included the solder resistance between the HTS rotor bars and the HTS end-rings, R_c . The equivalent circuit of the above resistances is shown in Fig. 3. Therefore, the HTS rotor bar resistance, R_r , is expressed as follows:

$$R_r = R_s // R_{ag} + R_c \quad (3)$$

Using Eq. (3), both losses of superconductor (R_s) and normal conductor (R_{ag} and R_c) can be estimated. Note that almost DC current flows in the HTS rotor windings in the synchronous speed rotation mode, the AC loss and the coupling loss is small correspondingly.

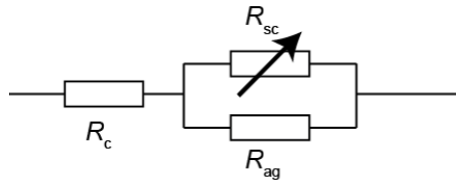


Fig. 3 Equivalent circuit of HTS rotor bars (R_{sc} : superconducting layer resistance obtained from Eqs. (1) and (2), R_{ag} : silver layer resistance, R_c : solder resistance between HTS rotor bars and HTS end-rings)

2.3 Thermal property

The thermal property values of the materials used in the 20 kW class HTS-ISM (77 K) are presented in Table II [20-22], and these values were used for the thermal analysis. The temperature dependencies of the aforementioned values were also considered in the thermal analysis.

It should be noted that the thermal diffusion time constant of the rotor teeth (0.731 s) was more than 7 times higher than that of the HTS (Bi-2223) rotor bars (0.104 s), and the heat generated in the HTS rotor bars could be immediately removed to the rotor core, when the thermal resistance

between them was sufficiently small.

Table II Materials used in 20 kW class HTS-ISM (77 K) and their thermal property values [20-22]

Item	Shaft	Rotor			Stator			Sleeve
		yoke	teeth	bar	yoke	teeth	Coil	
Material	SUS304	35JN210	35JN210	Bi-2223	35JN210	35JN210	Copper	SUS304
Volume (mm ³)	208131	455517	362971	157563	1402071	366077	348037	699319
Thermal conductivity (W/m/K)	14.8	92.6	92.6	159	92.6	92.6	755	14.8
Heat capacity (J/K)	792	497	396	96	1528	399	15260	2662
Thermal resistance (mW/K)	-	12.2	1.85	1.07	6.24	2.04	0.25	9.67
Thermal diffusion time constant (s)	-	6.081	0.731	0.104	9.536	0.814	3.820	25.744

3. Analysis method

3.1 Nonlinear voltage equations and equation of motion

The rotating characteristics of the HTS-ISM can be discussed based on the voltage equations and equation of motion. For the voltage equations, the three-phase electrical quantities are usually transformed to two-axis quantities to allow intuitive and easy understanding of the motor characteristics [23]. In this study, a static stationary orthogonal (ab-axis) coordinate system was considered. Note that the rotor structure of the HTS-ISM was a squirrel cage, and the corresponding equations are expressed as follows:

$$\begin{bmatrix} v_{as} \\ v_{bs} \\ 0 \\ 0 \end{bmatrix} = \begin{bmatrix} R_s + L_s \frac{d}{dt} & 0 & M \frac{d}{dt} & 0 \\ 0 & R_s + L_s \frac{d}{dt} & 0 & M \frac{d}{dt} \\ M \frac{d}{dt} & \frac{P}{2} \omega_m M & R_r + L_r \frac{d}{dt} & \frac{P}{2} \omega_m L_r \\ -\frac{P}{2} \omega_m M & M \frac{d}{dt} & -\frac{P}{2} \omega_m L_r & R_r + L_r \frac{d}{dt} \end{bmatrix} \begin{bmatrix} i_{as} \\ i_{bs} \\ i_{ar} \\ i_{br} \end{bmatrix} \quad (4)$$

where v and i are the voltage and current, respectively. The subscripts ‘a’ and ‘b’ denote the a- and b-axis values, respectively, and the subscripts ‘s’ and ‘r’ denote the stator and rotor values, respectively. Furthermore, R , L , and M correspond to the resistance, self-inductance and, mutual inductance, respectively; ω_m is the mechanical angular frequency; d/dt is the time operator; and P is the pole number, which was fixed to 4 in this study. Using Eq. (4), the torque, τ , can be expressed as follows:

$$\tau = \frac{P}{2} M (i_{bs} i_{ar} - i_{as} i_{br}) \quad (5)$$

The superconducting properties of the HTS rotor windings are taken to be indicated by the R_r of Eq. (4). That is, the nonlinearity of R_r is calculated from Eqs. (1), (2) and (3). In a previous study, we demonstrated that the nonlinear behaviour of R_r is crucial for stable rotation of the HTS-ISM [24]. For example, if the value of R_r is simply taken to be 0, the motor cannot begin rotation because no electromotive force is generated in the rotor windings. Then, the flux flow curve in Eq. (1) is crucial for starting. Such nonlinear resistance is also important for realise stable rotation against variable speed control.

The rotating characteristics of the motor are expressed as follows:

$$\tau = J \frac{d\omega_m}{dt} + D\omega_m + \tau_{load} \quad (6)$$

where J and D are, respectively, the moment of inertia and damping coefficient of the rotor, and τ_{load} is the loaded torque.

We can calculate the dynamic characteristics of the HTS-ISM by combining Eqs. (1)-(6), and have already reported the accuracy of their analysis [17,18].

3.2 Thermal equivalent circuit

Transient thermal analysis was also performed based on the thermal equivalent circuit. Fig. 4 illustrates the circuit developed for the 20 kW class HTS-ISM, which consists of heat flow, thermal resistance, and heat capacity elements. We considered two circuits parallel to the radial direction, i.e., with and without slots. Although the number of stator slots (48) differed from the number of rotor slots (38), we assumed the same number (38) for simplicity. The validity of this assumption is discussed below, through comparison with the results of a 3D-FEA.

Furthermore, we assumed that the heat leakage of the shaft from outside (room temperature) was 44 W; this value was estimated based on an experiment. The Joule losses for both slots of the rotor (HTS) and stator (Cu) were considered. The iron losses of the cores were calculated using two dimensional FEA analysis of Fig. 1 (JMAG designer[®] : JSOL Corp., Japan) for various input voltages and frequencies, and used for the multidisciplinary analysis.

In the considered design, the stator sleeve is cooled by means of the cryocooler (500 W@80 K). Therefore, the following equation was taken to represent the temperature dependence of the cryocooler cooling power, P_c :

$$P_c = 12.5 \times (T - 40\text{K}) \quad (\text{W}) \quad (7)$$

That is, the lowest realised temperature was assumed to be 40 K.

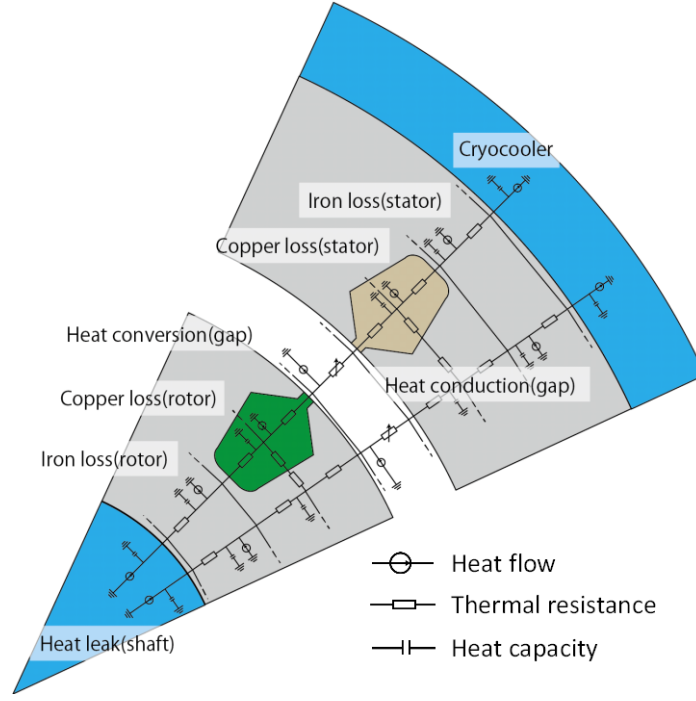


Fig. 4 Thermal equivalent circuit of 20 kW class HTS-ISM

3.3 Expression of cooling in air-gap

We considered two kinds of gaseous coolant heat transfer in the air-gap. The first one was the radial-direction heat transfer produced by the rotation of HTS rotor (Q_r), and the second one is the axial-direction heat transfer produced by axial flow of a gaseous coolant (Q_a). Q_r is expressed as follows [25]:

$$Q_r = UA(T_r - T_s) \quad (\text{W}) \quad (8)$$

$$\frac{U\delta}{\lambda} = 0.21 \left(\frac{v_r^2 \delta^2}{v^2} \frac{\delta}{r} P_r \right)^{1/4} \quad (-) \quad (9)$$

where T_r and T_s are the surface temperatures of the rotor and stator, respectively; A and r are, respectively, the external surface area and radius of the rotor; δ is the air-gap length; v_r is the circumferential speed of the rotor; P_r is the Prandtl number; U is the heat transmission rate; λ is the gas thermal conductivity; and ν is the gas kinematic viscosity coefficient of the gaseous coolant.

In addition, Q_a is expressed as follows [26]:

$$Q_a = hA(T_r - T_a) \quad (\text{W}) \quad (10)$$

$$h \frac{D_e}{\lambda} = 0.0015 \left(1 + 2.3 \frac{D_e}{L} \right) \left(\frac{D_s}{D_r} \right)^{0.45} \left(\frac{v_a D_e}{D_r} \right)^{0.8} P_r^{1/8} \quad (-) \quad (11)$$

where $D_e (= 2\delta)$ is the equivalent diameter; v_a is the axial flow velocity of gaseous coolant; h is the heat transfer coefficient; L is the distance from the heating point; and D_r and D_s are the outer diameters of the rotor and stator, respectively.

Fig. 5 is a schematic diagram of Q_r and Q_a . We assumed that the cooling characteristics of the gaseous coolant in the air-gap are a superposition of Q_r and Q_a .

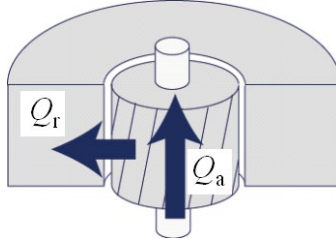


Fig. 5 Schematic diagram of radial direction heat transfer (Q_r) and axial direction heat transfer (Q_a) of gaseous coolant in HTS-ISM air gap

3.4 Multidisciplinary analysis

By combining the equations presented in sections 3.1, 3.2, and 3.3, multidisciplinary analysis was performed to investigate the transient cooling and rotating characteristics of the HTS-ISM. A flow chart of the analysis procedure is shown in Fig. 6. First, the rotation speed, frequency, and voltage were determined as the input information. Then, the input and output quantities, e.g., the input power and mechanical output, were obtained from the nonlinear voltage equations and equation of motion (section 3.1). Using the above quantities, the Joule losses were calculated and the

corresponding temperature was obtained from the thermal equivalent circuit (sections 3.2 and 3.3). From the calculated temperature, the rotor resistance of the HTS windings could be obtained and used for the next time step.

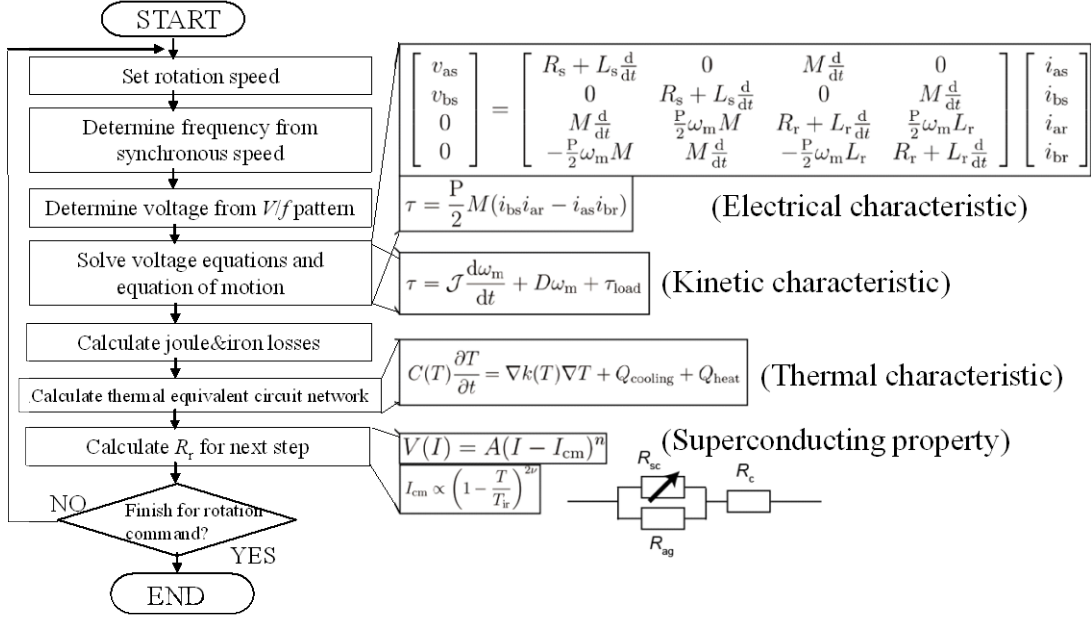


Fig. 6 Flow chart of multidisciplinary analysis procedure for 20 kW class HTS-ISM

4. Results and discussion

4.1 Validation of thermal equivalent circuit by comparison with 3D-FEA results

First, the accuracy of the thermal equivalent circuit was validated through comparison with a 3D-FEA model. Fig. 7 shows the 3D-FEA model used in this study, which was developed using JMAG designer[®]. The cooling power (P_c : Eq. (7)) was taken on the outer periphery of the sleeve as the thermal boundary condition.

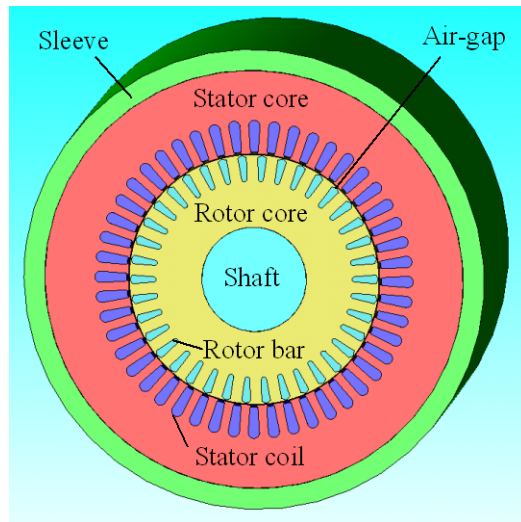
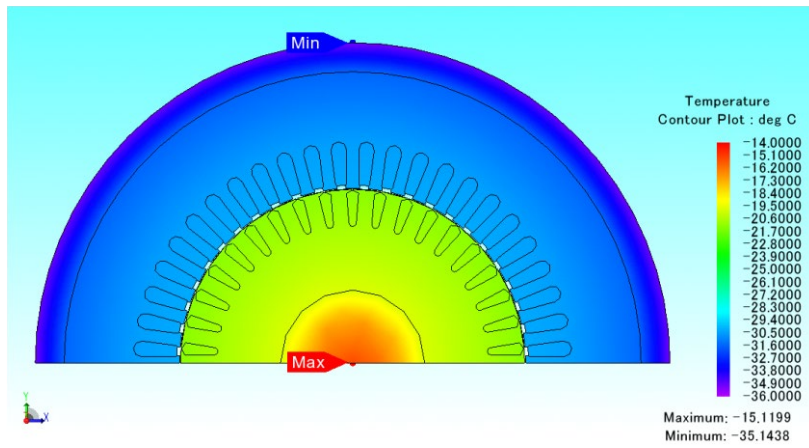


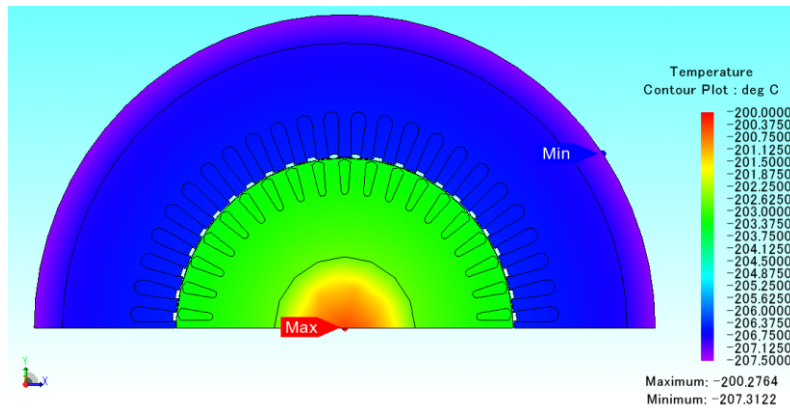
Fig. 7 3D-FEA model for thermal analysis of 20 kW class HTS-ISM (The outermost surface of the sleeve is cooled by a cryocooler and the air-gap between the stator core and rotor core is cooled by gaseous coolant. The heat intrusion from the outside is related to the shaft.)

Figs. 8 (a) and (b) show the temperature contours of the motor cross-section under the no-load condition, which were obtained from the 3D-FEA. The motor was cooled from room temperature, and the temporal variation of the temperature was analysed for 30000 s. As Fig. 8 (a) shows, the stator and rotor temperatures were approximately 244 K and 252 K, respectively, for the elapsed time of 1000 s. The shaft temperature, however, still exhibited a higher value, i.e., approximately 258 K, due to heat intrusion from outside. The motor reached its thermal equilibrium state when the cooling time reached 30000 s, and the corresponding temperature contour is shown in Fig. 8 (b). At that time, the shaft and sleeve temperatures were 71 K and 66 K, respectively; these values are sufficiently low for safe operation.

Note that the spatial distribution of the temperature was symmetrical in the circumferential direction of the motor. That is, the temperature was distributed in the radial direction only, and this result indicates the validity of the thermal equivalent circuit analysis. Next, the analysis results acquired from the thermal equivalent circuit were compared with the above results.



(a) Elapsed time: 1000 s



(b) Elapsed time: 30000 s

Fig. 8 3D-FEA temperature contour results starting from room temperature

Fig. 9 shows semi-logarithmic plots of the temperature vs. elapsed time characteristics obtained from the 3D-FEA and the thermal equivalent circuit. As apparent from this figure, the temperature traces of both the 3D-FEA and the thermal equivalent circuit exhibit reasonable agreement; thus, the validity of the circuit is apparent. The temperature differences between these plots in the steady state (30000 s) were 3.1 K for the sleeve (FEA: 66.1 K, equivalent circuit: 63.0 K) and 1.0 K for the shaft (FEA: 71.4 K, equivalent circuit: 70.4 K).

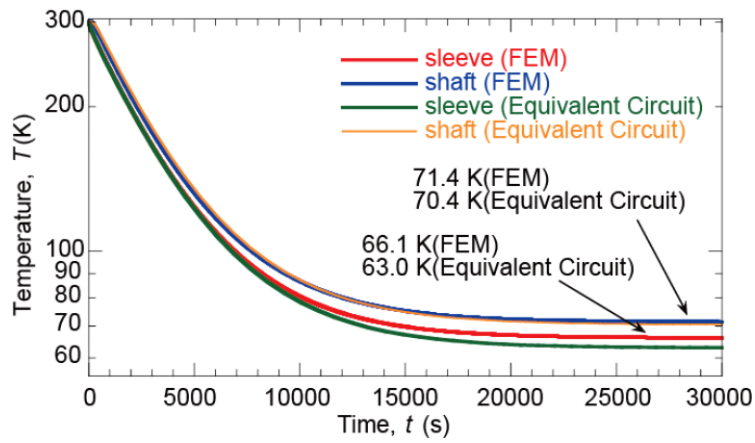
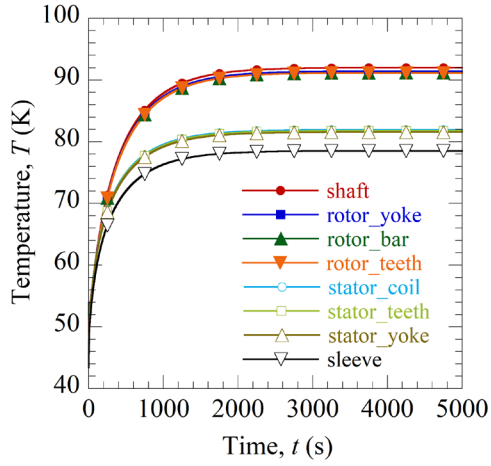


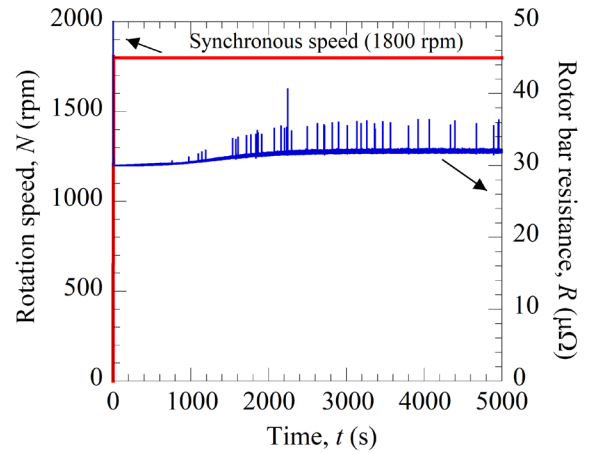
Fig. 9 Comparison of cooling characteristics of 20 kW class HTS-ISM given by 3D-FEA and thermal equivalent circuit

4.2 Transient characteristics

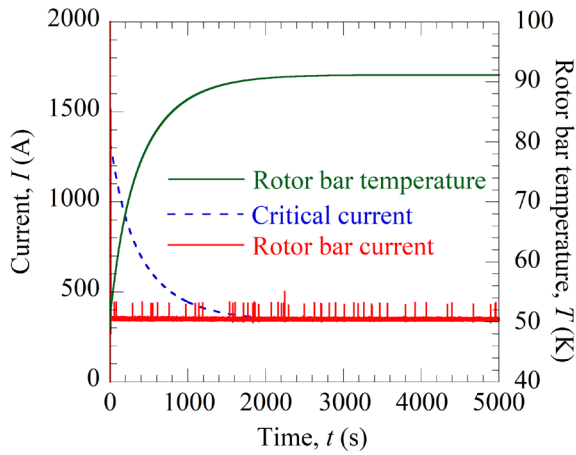
The transient cooling and rotating characteristics were investigated via the proposed multidisciplinary analysis procedure (Fig. 6). After the motor reached its steady state without excitation (the system's lowest temperature), the analysis was initiated. The synchronous rotation speed and the load torque at steady state were set to 1800 rpm (60 Hz) and 26.5 Nm, respectively. The corresponding mechanical output was 4.995 kW (25% of the rated output (20 kW)). Note that this rotation mode is most likely to remain throughout the entire operation of a typical EV system. We selected an input line voltage of 100 V at 60 Hz. The axial flow velocity of the gaseous coolant in Eq. (11), v_a , was assumed to 2.4 m/s in this study. Based on the above condition, the motor speed was increased from 0 to 1800 rpm for 10 s with an excitation rate of $V/f = 100 \text{ V}/60 \text{ Hz}$. Then, the motor characteristics were simulated.



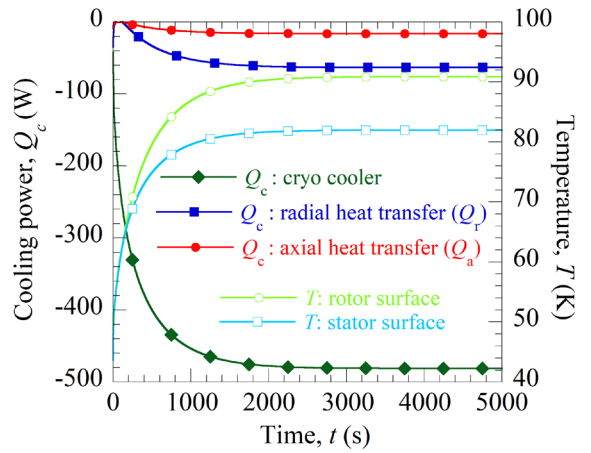
(a) Temperature



(b) Rotation speed and rotor bar resistance



(c) Rotor bar current, temperature and critical current



(d) Cooling power and temperature

Fig. 10 Analysis results for transient cooling and rotating characteristics of a 20 kW class HTS-ISM cooled by a cryocooler and gaseous coolant. The rotation speed was increased from 0 to 1800 rpm (60 Hz) for 10 s, and the steady state load torque was 26.5 Nm (4.995 kW) at 100 V and 60 Hz.

Fig. 10 shows the analysis results for the cooling and rotating characteristics of the motor. As apparent from Fig. 10(a), the stator and rotor temperatures reached 78.5 -81.9 K and 91.2 -92.0 K,

respectively, at $t = 5000$ s. That is, the temperature difference between the rotor and stator was approximately 11 K in the steady state.

Fig. 10(b) shows the corresponding rotor bar resistance with the rotation speed as functions of time. As apparent from this figure, the rotor bar had a resistance value of approximately $30 \mu\Omega$ in the initial state, which then gradually increased because of the temperature rise at $t > 1000$ s. This resistance value is largely attributed to the ohmic resistance of R_{ag} and R_c (see Fig. 3 and Eq. (3)). As described in section 3.1, the conventional (normal conducting) induction motor tends to be unstable rotation state against external disturbance such as temperature fluctuation, when the rotor bar resistance is ohmic and lower. Nevertheless, the HTS-ISM maintained stable rotation at $t > 1000$ s. The reason for such stable rotation is a spike-like rotor bar resistance that is shown in the same figure. That is, the steep (nonlinear) flux-flow resistance (see Fig. 2 and Eq. (1)) guaranteed the stable rotation by behave as a damping resistance [24]. In other words, the nonlinear resistance of the HTS rotor bar is extremely important for stable rotation of the motor. Fig. 10(c) shows the rotor bar current and the temperature trends over time. The critical current of the bar, which varies with temperature, is also plotted for reference. The cause of the spike-like current is the same as that of the rotor bar resistance (Fig. 10(b)).

Fig. 10(d) shows the cooling power of the cryocooler and the gaseous coolant at the air-gap as functions of time. The temperature traces of the rotor and stator are also plotted. The cryocooler cooling power increased with the temperature and then reached approximately 480 W in the steady state. However, the cooling power of the air-gap coolant was lower than that of the cryocooler. That is, even Q_r was approximately 60 W in the steady state. Furthermore, Q_a was quite small, and was not practically effective. As mentioned above, the axial direction gas flow was assumed to be 2.4 m/s in this study; thus, greater flow speed was required to improve the air-gap cooling performance. Importantly, the validity of the assumed expressions for the air-gap cooling, i.e., Eqs. (8)-(11), has not yet been experimentally elucidated; this validation is a very important topic for our future

research. In any case, the developed analysis procedure realises a method for investigating the transient cooling and rotating characteristics of the HTS-ISM.

5. Conclusion

In this study, we developed a multidisciplinary analysis procedure for the transient cooling and rotating characteristics of an HTS-ISM, which couples the nonlinear voltage equations, equation of motion, and thermal equivalent circuit. The validity of the thermal equivalent circuit was first clarified through comparison with 3D-FEA results. Using the developed procedure, the transient characteristics were analysed for a 20 kW class HTS-ISM, of which the outermost surface of the stator was cooled by a cryocooler and the rotor was cooled using the assumed air-gap gaseous heat transfer. This case study demonstrated that temporal variation of the various quantities of the HTS-ISM, e.g., the current, losses, output power, rotation speed, temperature, and cooling power, can be quantitatively analysed using the proposed approach. Hence, the rotating and cooling characteristics can be comprehensively discussed and optimised. Using our analysis procedure, we can study the optimal cooling structure and method for the HTS-ISM.

Acknowledgements

We would like to thank Dr. R. Nishino and Mr. K. Ikeda for their valuable discussions. We are also grateful for the assistance provided by Dr. F. Kucuk and Ms. S. Yamada. This work was supported by the Japan Science and Technology Agency under the Advanced Low Carbon Technology Research and Development Program (JST-ALCA), Japan.

References

- [1] Greg S, Bruce G, Swarn SK. The performance of a 5 MW high temperature superconductor ship propulsion motor. *IEEE Trans Appl Supercond* 2005; 15(2): 2206-2209
- [2] Gamble B, Snitchler G, MacDonald T. Full Power Test of a 36.5 MW HTS Propulsion Motor. *IEEE Trans Appl Supercond* 2011; 21(3): 1083-1088
- [3] Frank M, Frauenhofer J, van Hasselt P, Nick W, Neumueller H-W, Nerowski G. Long-term operational experience with first Siemens 400 kW HTS machine in diverse configurations. *IEEE Trans Appl Supercond* 2003; 13(2): 2120-2123
- [4] Fukaya A, Tsuda T, Oota T. Progress in motor with superconducting armature windings-axial-gap synchronous motors cooled by liquid nitrogen-. *TEION KOGAKU (J Cryo Super Soc Jpn)* 2012; 47(6): 370-376 (in Japanese)
- [5] Yanamoto T, Izumi M, Umemoto K, Oryu T, Murase Y, Kawamura M. Load test of 3-MW HTS motor for ship propulsion. *IEEE Trans Appl Supercond* 2017; 27(8): 5204305
- [6] Moon H, Kim Y-C, Park H-J, Yu I-K, Park M. An introduction to the design and fabrication progress of a megawatt class 2G HTS motor for the ship propulsion application. *Supercond Sci Technol* 2016; 29: 034009
- [7] Miki M, Tokura S, Hayakawa H, Inami H, Kitano M, Matsuzaki H, Kimura Y, Ohtani I, Morita E, Ogata H, Izumi M, Sugimoto H, Ida T. Development of a synchronous motor with Gd–Ba–Cu–O bulk superconductors as pole-field magnets for propulsion system. *Supercond Sci Technol* 2006; 19: S494-S499
- [8] Miki M, Felder B, Tsuzuki K, Izumi M, Hayakawa H. Development of the cryo-rotary joint for a HTS synchronous motor with Gd-bulk HTS field-pole magnets. *J. Phys.: Conf. Ser.* 2010; 234: 032039
- [9] Masson PJ, Brown GV, Soban DS, Luongo CA. HTS machines as enabling technology for

all-electric airborne vehicles. *Supercond Sci Technol* 2007; 20: 748–756

[10] Luongo CA, Masson PJ, Nam T, Mavris D, Kim H, Brown GV, Waters M, Hall D. Next Generation More-Electric Aircraft: A Potential Application for HTS Superconductors. *IEEE Trans Appl Supercond* 2009; 19(3): 1055 - 1068

[11] Berg F, Palmer J, Miller P, Dodds G. HTS system and component targets for a distributed aircraft propulsion system. *IEEE Trans Appl Supercond* 2017; 27(4): 3600307

[12] Hoelzen J, Liu Y, Bensmann B, Winnefeld C, Elham A, Friedrichs J, Hanke-Rauschenbach R. Conceptual design of operation strategies for hybrid electric aircraft. *Energies* 2018; 11: 217

[13] Terao Y, Kong W, Ohsaki H, Oyori H, Morioka N. Electromagnetic design of superconducting synchronous motors for electric aircraft propulsion. *IEEE Trans Appl Supercond* 2018; 28(4): 5208005

[14] Oyama H, Shinzato T. Development of high-temperature superconducting DC motor for automobiles. *Research, Fabrication and Applications of Bi-2223 HTS Wires* (World Scientific) 2016: 485-494

[15] Yumoto K, Nakano K, Hiratsuka Y. Development of Stirling Cryocooler for Electric Bus Superconducting Motor. *TEION KOGAKU (J Cryo Super Soc Jpn)* 2016; 51(5): 164-170 (in Japanese)

[16] Nakamura T, Itoh Y, Yoshikawa M, Nishimura T, Ogasa T, Amemiya N, Ohashi Y, Fukui S, Furuse M. Tremendous enhancement of torque density in HTS induction/synchronous machine for transportation equipments. *IEEE Trans Appl Supercond* 2015; 25(3): 5202304

[17] Karashima T, Nakamura T, Ikeda K, Amemiya N, Yoshikawa M, Itoh Y, Terazawa T, Ohashi Y. Experimental and analytical studies on highly efficient regenerative characteristics of a 20-kW class HTS induction/synchronous motor. *IEEE Trans Appl Supercond* 2017; 27(4): 5202605

[18] Karashima T, Nakamura T, Ikeda K, Nishino R, Yoshikawa M, Itoh Y, Terazawa T. Improvement of the variable speed controllability of a 20 kW class high-temperature

superconducting induction/synchronous motor at no-load condition. IEEE Trans Appl Supercond 2018; 28(3): 5204105

[19] Matsushita T. Flux Pinning in Superconductors, Springer Series in Solid-State Sciences 2014

[20] https://tpds.db.aist.go.jp/index_en.html

[21] Rizzo E. Simulations for the optimization of high temperature superconductor current leads for nuclear fusion applications, KIT Scientific Publishing, Karlsruhe, 2013

[22] Choudendou-Teionkogaku Handbook. 1993, Ohm (in Japanese)

[23] Woodson DC, White HH. Electromechanical Energy Conversion, Wiley 1959

[24] Muranaka K, Nakamura T, Okajima S, Ogasa T, Amemiya N, Itoh Y. Experimental and Analytical Studies on Variable Speed Control of High Temperature Superconducting Induction/Synchronous Motor. IEEE Trans Appl Supercond 2016; 26(4): 5201205

[25] Tachibana F, Fukui S, Mitsumura H. Heat transfer in an annulus with an inner rotating cylinder. Trans JSME Ser (2), 1959; 25(156): 788-792 (in Japanese)

[26] Tachibana F, Fukui S, Mitsumura H. Convective heat transfer of the rotational and axial flow between two concentric cylinders. Trans JSME Ser (2), 1963; 29(204): 1360-1366 (in Japanese)